# Charge transport and thermopower in the electron-doped narrow gap semiconductor $Ca_{1-x}La_xPd_3O_4$

Kouta Kazama,[1] Masato Sakano,[2] Kohei Yamagami,[3] Takuo Ohkochi,[3] Kyoko Ishizaka,[2] Terumasa Tadano,[4] Yusuke Kozuka,[5] Hidetoshi Yoshizawa,[1] Yoshihiro Tsujimoto,[5] Kazunari Yamaura,[5] and Jun Fujioka[1,6]

[1]*Graduate School of Science and Technology, University of Tsukuba, Tsukuba, Ibaraki 305-8573, Japan*

[2]*Quantum-Phase Electronics Center and Department of Applied Physics, University of Tokyo, Bunkyo-ku, Tokyo 113-8656, Japan*

[3]*Japan Synchrotron Radiation Research Institute, Kouto Sayo, Hyogo 679-5198, Japan*

[4]*Research Center for Magnetic and Spintronic Materials (CMSM), National Institute for Material Science (NIMS), Sengen, Tsukuba 305-0047, Japan*

[5]*Research Center for Materials Nanoarchitechtonics (MANA), National Institute for Material Science (NIMS), Namiki, Tsukuba 305-0044, Japan*

[6]*Department of Materials Science, University of Tsukuba, Tsukuba, Ibaraki 305-8573, Japan*

(Received 13 April 2023; accepted 24 July 2023; published 11 August 2023)

We have investigated the charge transport property, thermoelectric effect, and electronic state for the electron-doped narrow gap semiconductor $Ca_{1-x}La_xPd_3O_4$ by means of the transport measurement, optical/photoemission spectroscopy, and *ab initio* calculation. The high-quality polycrystalline samples of $Ca_{1-x}La_xPd_3O_4$ were synthesized by using the high-pressure synthesis technique. In the undoped system $x = 0$, the optical conductivity spectra show a charge gap of about 0.1 eV, which is qualitatively consistent with the results of *ab initio* calculation. The electron doping causes the rapid reduction of resistivity $\rho_{xx}$, resulting in the metallic state at the doping level of as small as $x = 0.01$. On the other hand, the magnitude of Seebeck coefficient $|S|$ moderately decreases with increasing $x$. Consequently, the power factor $S^2/\rho_{xx}$ reaches about 7 $\mu W/K^2cm$ at 350 K at $x = 0.03$, which is much higher than that of hole-doped analog of $CaPd_3O_4$. Combined with the results of photoemission spectra and *ab initio* calculation, the large power factor in the present material likely originates from the relatively low resistivity, probably high electron mobility ($\sim$30 $cm^2/Vs$ at 350 K), due to the dispersive Pd $4d_{x^2-y^2}$ conduction band.

DOI: 10.1103/PhysRevMaterials.7.085402

## I. INTRODUCTION

The Seebeck effect is a typical thermoelectric effect, which has been utilized as a principle of commercial thermoelectric devices. The power factor is a measure of efficiency for the energy conversion, which is defined as $\sigma S^2$ with $S$ and $\sigma$ being the Seebeck coefficient and electrical conductivity, respectively. The semimetals or narrow gap semiconductors are known as typical thermoelectric materials with potentially high power factor [1–12]. In particular, they often show the metallic state with small carrier density and high carrier mobility, which is advantageous for simultaneously realizing the large Seebeck coefficient and high electrical conductivity. For example, there are a number of narrow gap semiconductors with power factor more than 30 $\mu W/K^2cm$ at room temperature, regardless of their quite different band structure [2,3,6,7]. In fact, some of them have already been incorporated into practical thermoelectric devices. However, they often include toxic elements or are chemically unstable at the operating temperature above room temperature.

In this regard, the semimetals or narrow gap semiconductors of transition metal oxide have a potential to overcome these issues. The $APd_3O_4$ ($A$ = Ca and Sr) is a candidate of narrow gap semiconductor with potentially high power factor. As shown in Fig. 1(a), this material crystallizes in the $NaPt_3O_4$-type crystal structure of cubic symmetry, which is composed of the three-dimensional network of corner shared $PdO_4$ plaquette [13,14]. The Pd ion takes nominally divalent state in the $4d^8$-electronic configuration, and the electronic states near the Fermi energy $E_F$ is mainly composed of the Pd $4d$ $e_g$ state. So far, there are several theoretical proposals about the possible electronic structure near $E_F$. On the basis of electronic structure calculation, the narrow gap opening has been proposed [15,16], but the possibility of Dirac semimetallic state protected by the crystal symmetry is also argued [17–19]. On the other hand, there are few experimental studies on the electronic state near $E_F$ [20], which has not yet been elucidated so far.

Nevertheless, the charge transport and thermoelectric property have been extensively explored in the hole-doped analog of $CaPd_3O_4$ [14,21–23]. For example, the relatively large Seebeck coefficient more than 100 $\mu V/K$ is observed at room temperature in the metallic state of $Ca_{1-x}Li_xPd_3O_4$ [21]. Unfortunately, the resistivity $\rho_{xx}$ is not sufficiently low due to the small carrier mobility about 1−10 $cm^2/Vs$. Consequently, the power factor is at most about 1.6 $\mu W/K^2cm$ at $x = 0.4$. A strategy to further improve the thermoelectric property is the electron doping into $CaPd_3O_4$. However, the electronic property for the electron-doped analog of $CaPd_3O_4$ has been rarely explored due to the difficulty of preparing high quality

 

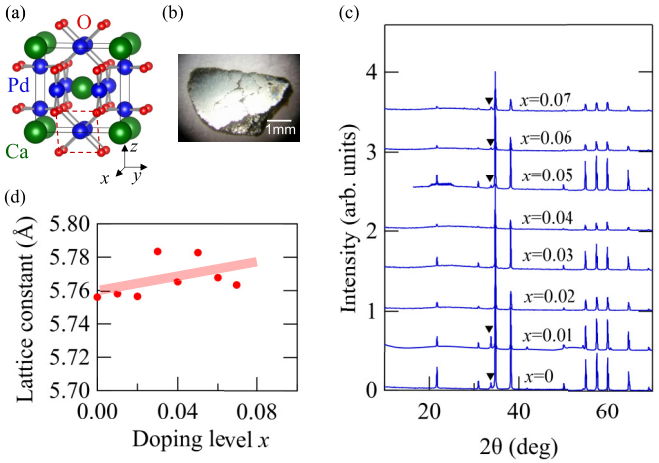


FIG. 1. (a) The crystal structure of $CaPd_3O_4$ [47]. The dashed line highlights the $PdO_4$ plaquette, which forms a three-dimensional network by sharing the corner oxygen ions. (b) Photograph of polycrystalline sample of $CaPd_3O_4$ synthesized by the solid state reaction under 2.5 GPa and 1300 °C. (c) Powder x-ray diffraction (XRD) for $Ca_{1-x}La_xPd_3O_4$ with $x = 0 - 0.07$ at room temperature. Each pattern is offset for clarity. The triangles indicate the diffraction from impurity phase (PdO). (d) The lattice constant derived from XRD for $Ca_{1-x}La_xPd_3O_4$.

samples. In this study, we synthesized the polycrystalline sample of electron-doped $Ca_{1-x}La_xPd_3O_4$ by means of the high pressure synthesis technique and explored their charge transport, thermoelectric property, and electronic structure. We found that the doping level of $x = 0.01$ induces the metallic state with relatively high electrical conductivity and Seebeck coefficient, resulting in the power factor of about 7 $\mu W/K^2cm$ at 350 K.

## II. EXPERIMENTAL METHODS AND ELECTRONIC STRUCTURE CALCULATION

To obtain polycrystalline samples of $Ca_{1-x}La_xPd_3O_4$ with minimal impurity phases such as PdO and Pd, we employed the high-pressure synthesis techniques. The starting materials CaO, PdO, and $La_2O_3$ were reacted under 2.5 GPa and 1300 °C by using a cubic anvil type facility. The samples are in the form of densely packed pellets with a few millimeters in size as shown in Fig. 1(b) [see also Fig. S1] [24]. We performed the x-ray diffraction by using commercial diffractometer (Rigaku MiniFlex) with Cu-K$\alpha_1$ and -K$\alpha_2$ as sources. The results of x-ray diffraction patterns show that the contamination of PdO and Pd is not significant [see Fig. 1(c)] and the lattice constant slightly increases with increasing $x$ [see Fig. 1(d)]. These are suitable for exploring the fine doping dependence of charge transport, thermoelectric property, and optical reflectivity. The nominal doping level $x$ at the time of synthesis is nearly identical to the results of energy dispersive x-ray spectroscopy (EDX) [see Fig. S1(e)]. Resistivity measurements were performed by the four-probe method in a physical property measurement system (Quantum Design). The Seebeck coefficient was measured while applying the temperature gradient by using a chip heater attached on one side of the sample [see Fig. S4]. The temperature gradient was measured by commercial thermocouples (chromel-constantan). The heater power was set so that the typical temperature difference between the thermocouple was about 1 K.

The optical reflectivity spectra were measured in the geometry of nearly normal incidence by using a Fourier transform spectrometer (grating-type monochromator) equipped with a microscope in the energy region of 0.02−0.7 eV (0.5−5 eV). In the region of 4−30 eV, we carried out the measurement at room temperature with use of synchrotron radiation at UV-SOR, Institute for Molecular Science (Okazaki). The optical conductivity spectra were derived by the Kramers-Kronig analysis. For the analysis, we adopted the Hagen-Rubens-type extrapolation below 0.02 eV and $\omega^4$-type extrapolation above 30 eV.

High-resolution photoemission spectroscopy (PES) measurements were performed under an ultrahigh vacuum less than $2 \times 10^{-8}$ Pa by using a He discharge lamp ($h\nu =$ 21.2 eV). The total energy resolution was set to 15 meV. Samples were fractured *in situ* and measured at 16 K. Core-level PES measurements were performed by using a monochromatized soft x-ray source ($h\nu = 900$ eV) at BL25SU of SPring-8 [25,26]. The total energy resolution was set to 110 meV. Samples were fractured *in situ* and measured at 20 K. The Fermi level was determined by measuring the Fermi cutoff of polycrystalline gold electrically connected to each sample.

We performed electronic structure calculations based on density functional theory using the *Vienna ab initio simulation package* (VASP) [27], which implements the projector augmented wave (PAW) method [28]. The plane-wave kinetic energy cutoff was set to 400 eV, and $6 \times 6 \times 6$ Γ-centered $k$ points were used for the Brillouin zone integration. The Heyd-Scuseria-Ernzerhof (HSE06) screened hybrid functional [29–31] was used, and the spin-orbit coupling was included in the calculation. To draw HSE06 band structures along high-symmetry lines, we performed Wannier interpolation using the Wannier90 code [32], where the Kohn-Sham states in the energy range of [−9:4] eV relative to the valence band maximum were used to construct maximally localized Wannier functions for the Pd 4$d$ and O 2$p$ orbitals. For these calculations, we assumed the crystal structure determined by the experiment.

## III. RESULTS AND DISCUSSION

Figure 2(a) shows the temperature dependence of resistivity for $Ca_{1-x}La_xPd_3O_4$ with $x = 0$. The resistivity shows the insulating behavior and divergently increases at low temperature. At high temperatures, the resistivity shows the activation-type behavior $\rho_{xx} \propto \exp(-E_g/2k_BT)$ with $E_g$ and $k_B$ being the effective band gap and Boltzmann constant, respectively [see Fig. 2(b)]. From the fitting, the effective band gap is estimated to be 0.11−0.13 eV. As shown in Fig. 2(c), the Hall resistivity $\rho_{yx}$ for $x = 0$ is nearly linear as a function of magnetic field, which shows a sizable temperature dependence. The Hall coefficient $R_H$ derived from the slope of $\rho_{yx}$ is negative in the measured temperature range (100−350 K), indicating that the electron-type carriers dominate the charge transport above 100 K. Assuming the single carrier model, the carrier density $n_H$ ($= |1/eR_H|$) appears to decrease from

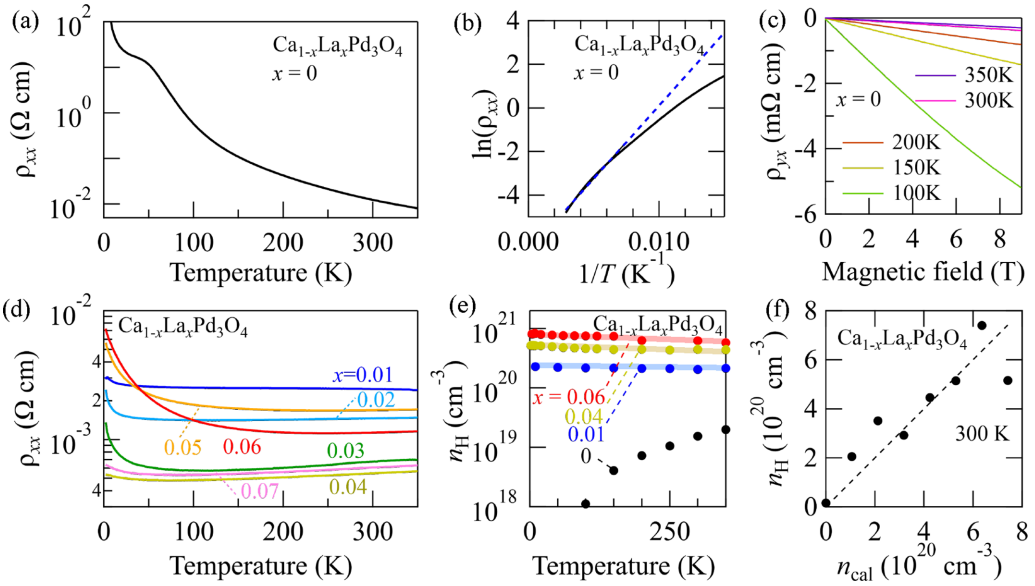


FIG. 2. (a) The temperature dependence of resistivity $\rho_{xx}$. (b) $\ln(\rho_{xx})$ plotted as a function of $1/T$. (c) The Hall resistivity ($\rho_{yx}$) for $Ca_{1-x}La_xPd_3O_4$ with $x = 0$. The dashed line in (b) is the fitting by the thermal activation model (see also the text). (d) Temperature dependence of $\rho_{xx}$ for $Ca_{1-x}La_xPd_3O_4$ with $x = 0.01 - 0.07$. (e) Temperature dependence of carrier density derived from the Hall coefficient $n_H$. (f) $n_H$ plotted as a function of nominal carrier density $n_{cal}$ expected from the La doping. The dashed line denotes the $n_H = n_{cal}$.

$1.5 \times 10^{19}$ $cm^{-3}$ at 300 K to $1.1 \times 10^{18}$ $cm^{-3}$ at 100 K with decreasing temperature [see Fig. 2(e)].

To clarify the electronic state, we investigated the optical conductivity $\sigma(\omega)$ spectra for $x = 0$. As shown in Fig. 3(a), $\sigma(\omega)$ spectra exhibit several peaks due to the optical phonons below 0.1 eV and the absorption band due to the interband transition above 0.12 eV. Moreover, a sharp peak with sizable temperature dependence is observed at 0.12 eV. The temperature variation of spectral shape for interband transition is moderate, suggesting that the electronic state does not significantly change with temperature. By linearly extrapolating the rising part of interband transition at 10 K, the charge gap is roughly estimated to be about 0.1 eV. Considering that the peak at 0.12 eV is located near the onset of interband transition and the peak width is much broader than that of optical

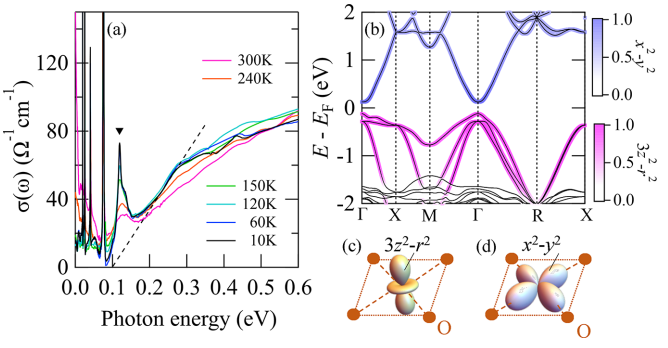


FIG. 3. (a) Optical conductivity $\sigma(\omega)$ spectra for $CaPd_3O_4$. The closed triangle denotes the peak at 0.12 eV. (b) The electronic structure for $CaPd_3O_4$. The color denotes the weight of Pd $4d_{3z^2-r^2}$ orbital (magenta) and Pd $4d_{x^2-y^2}$ orbital (blue). The illustration of (c) Pd $4d_{3z^2-r^2}$ orbital and (d) Pd $4d_{x^2-y^2}$ orbital in a $PdO_4$ plaquette. The closed circles denote the oxygen ions.

phonons, it may be attributed to the electronic excitation due to the impurity state located near the valence band top or exciton absorption.

More detailed insight into the electronic state can be obtained by the *ab initio* calculation. Figure 3(b) shows the calculated band structure for $CaPd_3O_4$. The calculated results show the band gap about 0.24 eV at the Γ point in the momentum space. The magnitude of band gap is slightly larger, but is of the same order as that determined from the optical conductivity spectra. The valence bands and conduction bands are mainly composed of Pd $4d_{3z^2-r^2}$ state and Pd $4d_{x^2-y^2}$ state, respectively [see also Fig. S2] [24]. In particular, near the Γ point, the conduction band is dispersive along all of the $\Gamma - R$, $\Gamma - M$, and $\Gamma - X$ lines. On the contrary, the dispersion of valence band of the highest energy is relatively flat along the $\Gamma - X$ and $\Gamma - M$ lines, while that along the $\Gamma - R$ line is dispersive. This difference can be qualitatively understood in terms of the orbital hybridization between the Pd $4d$ state and O $2p$ state in the $PdO_4$ plaquette; the Pd $4d_{x^2-y^2}$ state is hybridized with surrounding O $2p$ state more significantly than the Pd $4d_{3z^2-r^2}$ state [see also Figs. 3(c) and 3(d)], resulting in the larger band dispersion for the former [33]. In other words, the spatial anisotropy of Pd $4d$ orbital is likely crucial for the difference in the band dispersion between the conduction band and valence band, i.e., the electron-hole asymmetry in this material, which is rarely seen among conventional narrow gap semiconductors.

Next, we explored the charge transport and electronic state for the electron-doped $Ca_{1-x}La_xPd_3O_4$. As shown in Fig. 2(d), $\rho_{xx}$ rapidly decreases with increasing $x$, and the metallic state emerges at the doping level of as small as $x = 0.01$. In particular, the resistivity is reduced down to about 2−3 mΩcm for $x = 0.01$ and further decreases for $x \geqslant 0.03$. Such low resistivity is in contrast with the case of hole-doped analogs, wherein the resistivity is more than

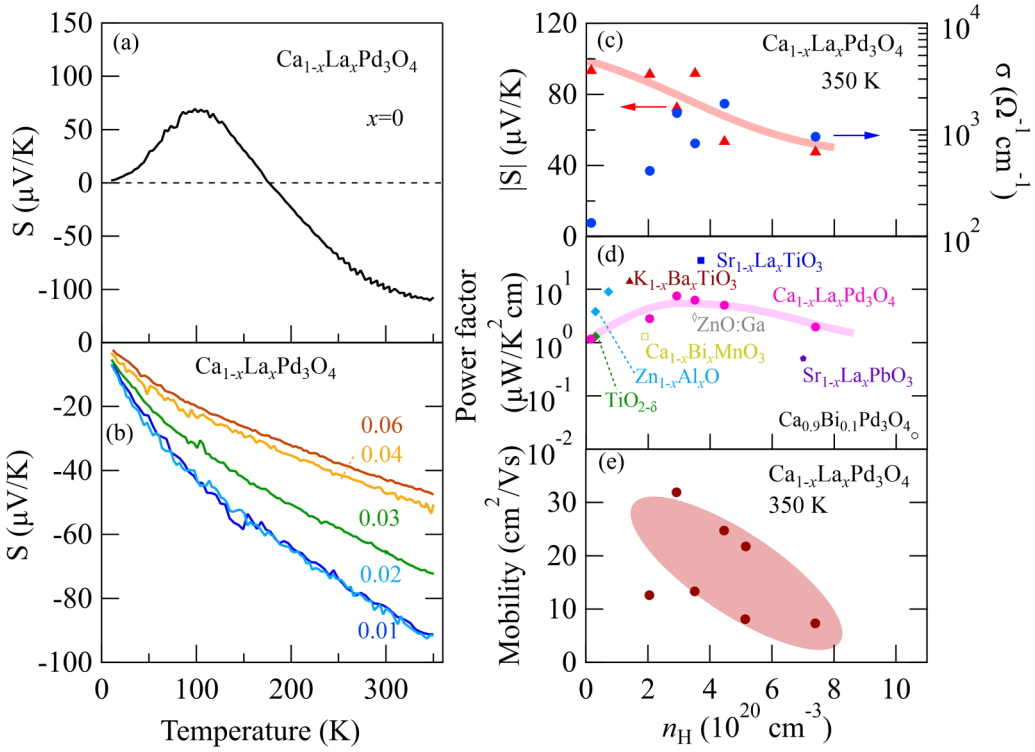


FIG. 4. Seebeck coefficient $S$ (a) for $CaPd_3O_4$ ($x = 0$) and (b) for $Ca_{1-x}La_xPd_3O_4$ with $x = 0.01 - 0.06$. (c) The absolute value of Seebeck coefficient $|S|$ and electrical conductivity $\sigma$ at 350 K. The solid curve is guide to the eyes. (d) The power factor $\sigma S^2$ for $Ca_{1-x}La_xPd_3O_4$ at 350 K as well as that near the room temperature (290 − 350 K) for various $n$-type oxides. (e) The carrier mobility for $Ca_{1-x}La_xPd_3O_4$ with $x = 0.01 - 0.07$.

10 mΩcm in the lightly doped region of $x \leqslant 0.05$ [21–23]. Figure 2(e) shows the temperature dependence of carrier density for $Ca_{1-x}La_xPd_3O_4$ with various $x$. In the doped systems, the carrier density is nearly temperature independent in contrast with the case of $x = 0$ [see also Fig. S3] [24]. In Fig. 2(f), the carrier density at 300 K is plotted against the nominal carrier density assuming that a trivalent La ion partially substituted into a divalent Ca ion introduces a conduction electron. The carrier density is nearly identical to the nominal carrier density, suggesting that the electron density is controlled by the doping level of La ions.

Figure 4(a) shows the temperature dependence of Seebeck coefficient for $CaPd_3O_4$. The sign of Seebeck coefficient is positive below 175 K, but becomes negative at higher temperatures. This suggests the so-called bipolar effect; the contribution from hole-type carriers (electron-type carriers) is dominant at low (high) temperatures. As shown in Fig. 4(b), for $x \geqslant 0.01$, the sign of Seebeck coefficient remains to be negative in all the temperature range from 10 K to 350 K. We plot the absolute value of Seebeck coefficient $|S|$ at 350 K as a function of carrier density in Fig. 4(c). $|S|$ moderately decreases with increasing the carrier density. In fact, $|S|$ for $x = 0.06$ ($n = 7 \times 10^{20}$ cm$^{-3}$) is more than one-third of the value for $x = 0$. On the contrary, the electrical conductivity $\sigma$ rapidly increases with increasing the carrier density [see Fig. 4(c)]; the electrical conductivity for $x = 0.03 - 0.04$ ($n = 3 - 4 \times 10^{20}$ cm$^{-3}$) is one order larger than that for $x = 0$. As a result, the power factor $\sigma S^2$ reaches a maximum around $n = 3 \times 10^{20}$ cm$^{-3}$ ($x = 0.03$), wherein the peak value is about 7 μW/K$^2$cm as shown in Fig. 4(d). This value is about four times the maximum in the hole-doped analog of $CaPd_3O_4$ [21,22], which is also relatively large compared with other $n$-type transition metal oxide semiconductors [34–42].

To clarify the electronic state in the electron-doped region, we explored the photoemission spectra for $Ca_{1-x}La_xPd_3O_4$ with $x = 0$, 0.03, 0.05, and 0.07. As shown in Fig. 5(a), the photoemission spectrum from the valence band onsets immediately below $E_F$ for $x = 0$. On the contrary, for $x \geqslant 0.03$, the threshold energy seems to be slightly lower, and a small kink due to the Fermi edge is observed at $E_F$ [see also Fig. S5] [24]. Here, we defined the valence band maximum (VBM) by linearly extrapolating the rising part of photoemission spectrum to the baseline [see Fig. 5(a)]. Figure 5(b) shows the VBM plotted as a function of $x$. The relative energy of VBM measured from $E_F$, i.e., $E - E_F$ monotonically decreases with increasing $x$.

We also explored the photoemission spectra of Pd $3d_{5/2}$ core level, which is located in a much deeper energy region. As shown in Fig. 5(c), the photoemission spectrum from the Pd $3d_{5/2}$ core level is composed of a peak and shoulder. The peak is assigned to the signal from the nominally divalent state $Pd^{2+}$, while the shoulder is likely attributed to that from the surface state and/or the tetravalent state $Pd^{4+}$ [43,44]. By fitting the spectra, we determined the relative energy of Pd $3d_{5/2}$ core level. As shown in Fig. 5(b), with increasing $x$, the relative energy of Pd $3d_{5/2}$ core level decreases similarly with that of the VBM. These results suggest that the photoemission peaks nearly uniformly shifts to deeper relative energy with increasing $x$. In other words, this means that $E_F$ increases in the scheme of rigid band picture as illustrated in Fig. 5(d); $E_F$

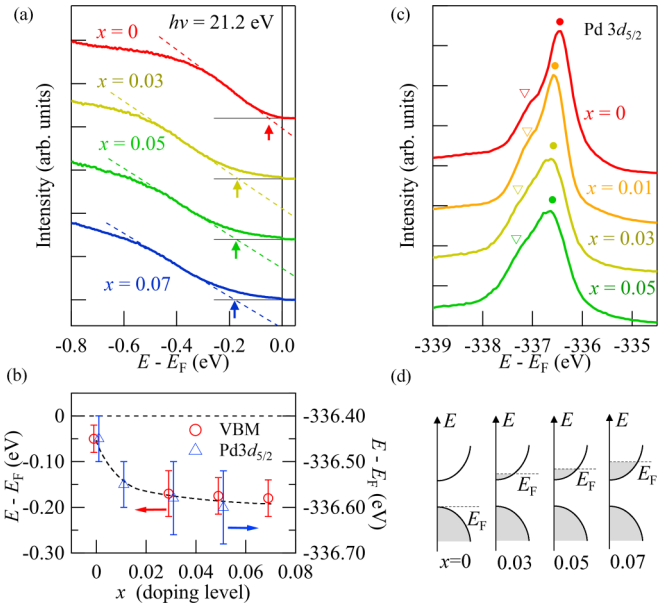


FIG. 5. (a) Valence band photoemission spectra for $Ca_{1-x}La_xPd_3O_4$ with $x = 0 - 0.07$. Each spectrum is offset for clarity. The horizontal (vertical) solid line denotes the baseline (Fermi energy). The dashed line is the extrapolation to estimate the valence band maximum (VBM), which is shown by arrows. (b) The energy of VBM and that of Pd $3d_{5/2}$ plotted as a function of $x$. (c) The core level photoemission spectra of $Ca_{1-x}La_xPd_3O_4$ with $x = 0 - 0.05$. The circles and triangles denote the main peak from Pd $3d_{5/2}$ state and the shoulder (see the text), respectively. Each spectrum is offset for clarity. (d) The illustration of density of state near the Fermi energy.

is almost located at the valence band top for $x = 0$, but rapidly moves above the conduction band minimum for $x \geqslant 0.01$. Such doping variation of electronic state is in contrast with the case of doped Mott insulator, in which the electronic state near $E_F$ significantly changes upon the electron/hole doping [45,46].

On the basis of these results, we consider the doping variation of charge transport and thermoelectric effect. For $x = 0$, it is likely that the hole-type carriers in the valence band or impurity state located near the VBM govern the transport at low temperatures. This is consistent with the positive sign of the Seebeck coefficient observed at low temperatures. On the contrary, near the room temperature, the thermally excited electrons in the conduction band likely dominate the transport property, resulting in the negative sign of the Seebeck coefficient and Hall coefficient. This is also consistent with the fact that the effective band gap is nearly identical to the charge gap determined from the optical conductivity spectra. We note that the previous study reports the positive Seebeck coefficient up to 500 K [21]. This discrepancy may be attributed to the difference in the Fermi energy, which is sensitive to the chemical off-stoichiometry of samples.

For $x \geqslant 0.01$, the doped electrons govern the charge transport in all the temperature range below 350 K. It is likely that the enhancement of power factor is attributed to the relatively large Seebeck coefficient while keeping the high electrical conductivity, probably the relatively high electron mobility in the lightly doped region. Indeed, as shown in Fig. 4(e), the electron mobility remains to be about 30 $cm^2/Vs$ even at 350 K for $x = 0.03$, which however decreases with increasing the carrier density due to the scattering from the doped La ions or degradation of crystallinity by chemical substitution. Note that the value in the lightly doped region is one order of magnitude higher than the value in the hole-doped analog about $1-10$ $cm^2/Vs$ [21]. The larger dispersion of conduction Pd $4d_{x^2-y^2}$ band may be crucial for the relatively high electron mobility and power factor in the electron doped $Ca_{1-x}La_xPd_3O_4$.

## IV. CONCLUSION

In conclusion, we have investigated the charge transport, electronic state, and thermoelectric effect of electron-doped $Ca_{1-x}La_xPd_3O_4$ by means of transport measurements, optical spectroscopy, *ab initio* calculation, and photoemission spectroscopy. We synthesized the high quality samples of $Ca_{1-x}La_xPd_3O_4$ by using the high pressure synthesis technique. For $CaPd_3O_4$ ($x = 0$), the temperature dependence of resistivity shows the insulating behavior, and the optical conductivity spectra show a charge gap of about 0.1 eV. The *ab initio* calculation suggests that the conduction band and valence band are mainly composed of the Pd $4d_{x^2-y^2}$ state with larger band dispersion and Pd $4d_{3z^2-r^2}$ state with smaller band dispersion, respectively. Upon the electron doping, the resistivity rapidly decreases with increasing $x$, and the metallic state emerges even at the small doping level of $x = 0.01$. Indeed, owing to the relatively high electron mobility ($\sim$30 $cm^2/Vs$), the electrical conductivity exceeds 1000 $\Omega^{-1}cm^{-1}$ in the lightly doped region for $x = 0.03-0.05$ even at 350 K. On the contrary, the magnitude of Seebeck coefficient moderately decreases with increasing $x$. Consequently, the power factor $\sigma S^2$ reaches about 7 $\mu W/K^2cm$ at 350 K for $x = 0.03 - 0.04$. Furthermore, the results of photoemission spectra suggest that the doped electrons occupy the conduction band in the scheme of the rigid band picture. It is likely that the enhanced power factor is attributed to the relatively high electron mobility due to the dispersive Pd $4d_{x^2-y^2}$ conduction band in this electron-doped oxide semiconductor.

## ACKNOWLEDGMENTS

We thank A. Oshima, T. Nakamura, and T. Koyano for the technical supports for measurements of the photoemission spectra and transport property. The synchrotron radiation experiments were performed at SPring-8 with the approval of the Japan Synchrotron Radiation Research Institute (JASRI) (Proposals No. 2022B1332 and No. 2022B2106). This work was partly supported by Grant-In-Aid for Science Research (Grants No. 18H01171, No. 19H01851, No. JP20H01834, No. 21K18813, and No. 22H01177) from the MEXT, by Nippon Sheet Glass Foundation for Materials Science and Engineering, Japan, by JST FOREST Program (Grant No. JPMJFR203D) and by the University of Tsukuba, Pre-Strategic Initiatives Development Center for High-Function and High-Performance Organic-Inorganic Spin Electronics. MANA is supported by World Premier International Research Center Initiative (WPI), MEXT, Japan.

[1] J. W. Sharp, E. C. Jones, R. K. Williams, P. M. Martin, and B. C. Sales, J. Appl. Phys. **78**, 1013 (1995).

[2] T. Caillat, M. Carle, P. Pierrat, H. Scherrer, and S. Scherrer, J. Phys. Chem. Solids **53**, 1121 (1992).

[3] J. W. G. Bos, H. W. Zandbergen, M.-H. Lee, N. P. Ong, and R. J. Cava, Phys. Rev. B **75**, 195203 (2007).

[4] Y. Pei, X. Shi, A. LaLonde, H. Wang, L. Chen, and G. J. Snyder, Nature (London) **473**, 66 (2011).

[5] C.-R. Wang, W.-S. Lu, L. Hao, W.-L. Lee, T.-K. Lee, F. Lin, I.-C. Cheng, and J.-Z. Chen, Phys. Rev. Lett. **107**, 186602 (2011).

[6] L. D. Zhao, G. Tan, S. Hao, J. He, Y. Pei, H. Chi, H. Wang, S. Gong, H. Xu, V. P. Dravid, C. Uher, G. J. Snyder, C. Wolverton, and M. G. Kanatzidis, Science **351**, 141 (2016).

[7] T. Inohara, Y. Okamoto, Y. Yamakawa, A. Yamakage, and K. Takenaka, Appl. Phys. Lett. **110**, 183901 (2017).

[8] J. M. Tomczak, J. Phys.: Condens. Matter **30**, 183001 (2018).

[9] A. Nakano, U. Maruoka, F. Kato, H. Taniguchi, and I. Terasaki, J. Phys. Soc. Jpn. **90**, 033702 (2021).

[10] K. Tsuruda, K. Nakagawa, M. Ochi, K. Kuroki, M. Tokunaga, H. Murakawa, N. Hanasaki, and H. Sakai, Adv. Funct. Mater. **31**, 2102275 (2021).

[11] T. Zhou, C. Zhang, H. Zhang, F. Xiu, and Z. Yang, Inorg. Chem. Front. **3**, 1637 (2016).

[12] J. Fujioka, M. Kriener, D. Hashizume, Y. Yamasaki, Y. Taguchi, and Y. Tokura, Phys. Rev. Mater. **5**, 094201 (2021).

[13] P. L. Smallwood, M. D. Smith, and H.-C. zur Loye, J. Cryst. Growth **216**, 299 (2000).

[14] K. Itoh and N. Tsuda, Solid State Commun. **109**, 715 (1999).

[15] I. Hase and Y. Nishihara, Phys. Rev. B **62**, 13426 (2000).

[16] A. Khan, Z. Ali, I. Khan, S. J. Asadabadi, and I. Ahmad, Bull. Mater. Sci. **39**, 1861 (2016).

[17] G. Li, B. Yan, Z. Wang, and K. Held, Phys. Rev. B **95**, 035102 (2017).

[18] S. M. L. Teicher, L. K. Lamontagne, L. M. Schoop, and R. Seshadri, Phys. Rev. B **99**, 195148 (2019).

[19] F. Tang and X. Wan, Front. Phys. **14**, 43603 (2019).

[20] B. H. Reddy, A. Ali, and R. S. Singh, J. Phys.: Condens. Matter **33**, 185502 (2021).

[21] S. Ichikawa and I. Terasaki, Phys. Rev. B **68**, 233101 (2003).

[22] T. C. Ozawa, A. Matsushita, Y. Hidaka, T. Taniguchi, S. Mizusaki, Y. Nagata, Y. Noro, and H. Samata, J. Alloys Compd. **448**, 77 (2008).

[23] L. K. Lamontagne, G. Laurita, M. Knight, H. Yusuf, J. Hu, R. Seshadri, and K. Page, Inorg. Chem. **56**, 5158 (2017).

[24] See Supplemental Material at http://link.aps.org/supplemental/10.1103/PhysRevMaterials.7.085402 for the sample characterization, transport property, and electronic state.

[25] Y. Senba, H. Ohashi, Y. Kotani, T. Nakamura, T. Muro, T. Ohkochi, N. Tsuji, H. Kishimoto, T. Miura, M. Tanaka, M. Higashiyama, S. Takahashi, Y. Ishizawa, T. Matsushita, Y. Furukawa, T. Ohata, N. Nariyama, K. Takeshita, T. Kinoshita, A. Fujiwara *et al.*, AIP Conf. Proc. **1741**, 030044 (2016).

[26] T. Muro, Y. Senba, H. Ohashi, T. Ohkochi, T. Matsushita, T. Kinoshita, and S. Shin, J. Synchrotron Rad. **28**, 1631 (2021).

[27] G. Kresse and J. Furthmuller, Phys. Rev. B **54**, 11169 (1996).

[28] G. Kresse and D. Joubert, Phys. Rev. B **59**, 1758 (1999).

[29] J. Heyd, G. E. Scuseria, and M. Ernzerhof, J. Chem. Phys **118**, 8207 (2003).

[30] J. Heyd, G. E. Scuseria, and M. Ernzerhof, J. Chem. Phys. **124**, 219906 (2006).

[31] A. V. Krukau, O. A. Vydrov, A. F. Izmaylov, and G. E. Scuseria, J. Chem. Phys. **125**, 224106 (2006).

[32] G. Pizzi, V. Vitale, R. Arita, S. Blügel, F. Freimuth, G. Géranton, M. Gibertini, D. Gresch, C. Johnson, T. Koretsune, J. Ibañez-Azpiroz, H. Lee, J.-M. Lihm, D. Marchand, A. Marrazzo, Y. Mokrousov, J. I. Mustafa, Y. Nohara, Y. Nomura, L. Paulatto *et al.*, J. Phys.: Condens. Matter **32**, 165902 (2020).

[33] M.-L. Doublet, E. Canadell, and M.-H. Whangbo, J. Am. Chem. Soc. **116**, 2115 (1994).

[34] T. Okuda, K. Nakanishi, S. Miyasaka, and Y. Tokura, Phys. Rev. B **63**, 113104 (2001).

[35] A. Sakai, T. Kanno, S. Yotsuhashi, H. Adachi, and Y. Tokura, Jpn. J. Appl. Phys. **48**, 097002 (2009).

[36] T. Tsubota, M. Ohtaki, K. Eguchi, and H. Arai, J. Mater. Chem. **8**, 409 (1998).

[37] K.-H. Jung, K. H. Lee, W.-S. Seo, and S.-M. Choi, Appl. Phys. Lett. **100**, 253902 (2012).

[38] D. Berardan, C. Byl, and N. Dragoe, J. Am. Ceram. Soc. **93**, 2352 (2010).

[39] M. Ohtaki, H. Koga, T. Tokunaga, K. Eguchi, and H. Arai, J. Solid State Chem. **120**, 105 (1995).

[40] I. Terasaki and T. Nonaka, J. Phys.: Condens. Matter **11**, 5577 (1999).

[41] H. Liu, H. Ma, T. Su, Y. Zhang, B. Sun, B. Liu, L. Kong, B. Liu, and X. Jia, J. Materiomics **3**, 286 (2017).

[42] I. Terasaki, S. Ichikawa, and S. Shibasaki, *Proceedings of the 23rd International Conference on Thermoelectrics* (Organizing committee of 23rd International Conference on Thermoelectrics, ICT2004, 2005), p. 094.

[43] L. P. A. Guerrero-Ortega, E. Ramírez-Meneses, R. Cabrera-Sierra, L. M. Palacios-Romero, K. Philippot, C. R. Santiago-Ramírez, L. Lartundo-Rojas, and A. Manzo-Robledo, J. Mater. Sci. **54**, 13694 (2019).

[44] L. S. Kibis, A. A. Simanenko, A. I. Stadnichenko, V. I. Zaikovskii, and A. I. Boronin, J. Phys. Chem. C **125**, 20845 (2021).

[45] M. Imada, A. Fujimori, and Y. Tokura, Rev. Mod. Phys. **70**, 1039 (1998).

[46] H. Wadati, D. Kobayashi, H. Kumigashira, K. Okazaki, T. Mizokawa, A. Fujimori, K. Horiba, M. Oshima, N. Hamada, M. Lippmaa, M. Kawasaki, and H. Koinuma, Phys. Rev. B **71**, 035108 (2005).

[47] K. Momma and F. Izumi, J. Appl. Cryst. **44**, 1272 (2011).